AIAA 99-0157

Turbulence Model Predictions of Extra-Strain Rate Effects in Strongly-Curved Flows

Christopher L. Rumsey and
Thomas B. Gatski
NASA Langley Research Center
Hampton, Virginia

Joseph H. Morrison
Analytical Services & Materials, Inc.
Hampton, Virginia

37th Aerospace Sciences Meeting & Exhibit
January 11-14, 1999/Reno, NV

TURBULENCE MODEL PREDICTIONS OF EXTRA-STRAIN RATE EFFECTS IN STRONGLY-CURVED FLOWS

Christopher L. Rumsey* and Thomas B. Gatski†
NASA Langley Research Center
Hampton, Virginia

Joseph H. Morrison‡
Analytical Services & Materials, Inc.
Hampton, Virginia

Abstract

The abilities of three types of turbulence models to accurately predict the effects of curvature on flow in a U-duct are studied. An explicit algebraic stress model performs better than one- or two-equation linear eddy viscosity models, although it is necessary to fully account for the variation of the production-to-dissipation-rate ratio in the algebraic stress model formulation. None of the turbulence models fully captures the suppressed turbulence near the convex wall or enhanced turbulence near the concave wall. However, a full Reynolds stress model predicts the suppressed turbulence near the convex wall. Some of the underlying assumptions used in the development of algebraic stress models are investigated and compared with the computed flow field from a full Reynolds stress model. Through this analysis, the assumption of Reynolds stress anisotropy equilibrium used in the algebraic stress model formulation is found to be suspect in regions of strong curvature.

1 Introduction

Many flow fields being calculated by computational fluid dynamics (CFD) codes are so complex that it can be difficult to determine the source of error in comparison with experiment. For example, the flow over a multi-element airfoil contains a wide variety of challenging physical processes, including confluent boundary layers, wakes in adverse pressure gradient, separated flows, possible unsteady flow, possible shock/boundary layer interactions, and significant streamline curvature. Current state-of-the-art CFD codes do not predict certain aspects of the physics of multi-element airfoil flows accurately enough for design studies.[1] Turbulence models are often assigned the blame, but due to the complexities of the multi-element flow field it is not certain why the models are deficient. (In fact, many other factors may contribute, such as improper transition modeling or lack of 3-D effects in 2-D computations.) For turbulence model developers to determine how to improve their models, it is important to isolate and quantify the various effects of significance to the problem of interest, and to evaluate turbulence models in such flows.

For example, the flow off the main element on a multi-element configuration can turn as much as 30°–40° as it passes over the flap. It is possible that such turning (convex curvature) has an impact on the Reynolds shear stresses in that region, which in turn may affect the mean flow over the flap. Preliminary comparisons of computed Reynolds shear stresses with experimentally measured values in the flap region indicate that some discrepancies exist.[2] Currently, it is uncertain whether the disagreement is due to the turbulence model itself, or whether other factors are to blame. In particular, note that the δ/R parameter (boundary layer thickness over radius of curvature) that defines the turning of the flow over the flap can be on the order of 0.01 to 0.1, depending on the particular configuration and whether the main element wake is included in the determination of δ. In general, $\delta/R < 0.01$ represents very mild curvature, whereas $0.1 < \delta/R < 1$ represents moderate to strong curvature.[3]

Monson and Seegmiller[4] and Monson et al.[5] performed a nominally 2-D experiment on flow through

*Senior Research Scientist, Aerodynamic and Acoustics Methods Branch, Fluid Mechanics and Acoustics Division, Senior Member AIAA.

†Senior Research Scientist, Aerodynamic and Acoustics Methods Branch, Fluid Mechanics and Acoustics Division.

‡Senior Research Scientist, Senior Member AIAA.

a U-duct (with aspect ratio 10), and evaluated the abilities of several turbulence models to predict both the mean flow (velocity profiles, skin friction, and surface pressure) and turbulence quantities (turbulent kinetic energy and Reynolds shear stress). The curvature was strong in this setup, with δ/R approximately 0.5 around the inner wall. The U-duct is representative of many internal flows of engineering interest, such as flow in the turnaround duct in the Space Shuttle main engine powerhead. However, the U-duct is also of interest for any flow, internal or external, that experiences curvature, because it is a well-defined nominally 2-D experiment. It is an ideal test case to isolate the effect of curvature and to evaluate the ability of existing turbulence models to predict the physics of curvature. Many other curved duct flow experiments have been performed, e.g., Refs. 6–10, but most either do not explicitly define the outer wall geometry or else have lower aspect ratios (and hence more significant 3-D effects). These ambiguities limit the usefulness of such studies for turbulence model validation.

In Monson et al.,[5] seven isotropic eddy viscosity turbulence models (one algebraic and six K-ε models) evaluated against the Monson and Seegmiller[4] data met with varying degrees of success regarding prediction of skin friction, but none of them consistently predicted the measured mean velocities downstream of the turn or the turbulence quantities in or downstream of the turn. Luo and Lakshminarayana[11] computed the same configuration using four levels of turbulence model approximations: a linear eddy viscosity K-ε model, a nonlinear (NL) K-ε model, an implicit algebraic Reynolds stress model (ARSM), and a full Reynolds stress model (RSM). All models were linked to a near-wall one-equation model near $y^+ = 70$. The eddy viscosity model predicted higher Reynolds shear stress over the convex wall, resulting in a smaller extent of separation. The other models were better, but only the RSM predicted nearly complete suppression of Reynolds shear stress over the convex wall as seen in the experiment. All four models predicted too slow a recovery downstream of flow reattachment.

Many other computations of turbulent curved flows for similar configurations have been done, only a few of which are mentioned here. Rodi and Scheuerer[12] examined three extensions to the K-ε model, including an algebraic stress model without curvature-specific empiricism. They found that this algebraic stress model gives the best overall agreement in the curved part of the flow. Luo and Lakshminarayana[13] found that although a Reynolds stress model can successfully capture the large damping of turbulence near a convex wall, it underpredicts the enhancement of turbulence near a concave wall; in order to capture the amplification, they concluded that the standard ε equation needs to be modified. Iacovides et al.[14] evaluated an algebraic stress model and Shima[15] evaluated a Reynolds stress model; both methods were found to be superior to linear two-equation models for curved flows.

In Rumsey et al.,[16] several turbulence models were evaluated for multi-element airfoil flows. Two of these models, the one-equation Spalart-Allmaras[17] (S-A) and the two-equation Menter[18] shear-stress transport (SST) K-ω, are isotropic eddy viscosity models that are used extensively by the aerospace community. The third model is the explicit algebraic stress model (EASM) of Gatski and Speziale.[19] For the flow fields explored in Rumsey et al.,[16] all three models showed minor differences from each other, but they also each showed gross deficiencies in comparison with experiment, attributed primarily to poor transition modeling over the slat. Because of the gross deficiencies, it proved to be impossible to distinguish among the turbulence models themselves or recommend areas for turbulence model improvement.

In the current work, we apply the same three turbulence models to flow in the 2-D U-duct, and investigate their ability to model the physics due to strong curvature. Furthermore, recent advances in the explicit algebraic stress formulation[20–23] are explored in relation to the U-duct flow. Through this study, flow field curvature — one of the component physical processes of possible importance in the flow over multi-element configurations — is explored. Separate on-going work focuses on other aspects, including wake development in an adverse pressure gradient and transition. By exploring the component pieces, we hope to address specific deficiencies in existing turbulence models and develop better turbulence models in the future.

2 Description of the Codes

The computer code CFL3D[24] solves the three-dimensional, time-dependent, Reynolds averaged Navier-Stokes equations with an upwind finite-volume formulation. It can solve flows over multiple-zone grids that are connected in a one-to-one, patched, or overset manner, and can employ grid sequencing, multigrid, and local time stepping when accelerating convergence to steady state. Upwind-biased spatial differencing is used for the inviscid terms, and flux limiting is used to obtain smooth solutions in the vicinity of shock waves, when present. Viscous terms are centrally differenced, and cross-

diffusion terms are neglected. The flux-difference-splitting (FDS) method of Roe[25] is employed to obtain inviscid fluxes at the cell faces.

The CFL3D code is advanced in time with an implicit approximate factorization method. The implicit derivatives are written as spatially first-order accurate, which results in block tridiagonal inversions for each sweep. However, for solutions that utilize FDS, the block tridiagonal inversions are further simplified using a diagonal algorithm with a spectral radius scaling of the viscous terms.

The turbulence models are solved uncoupled from the mean flow equations. Descriptions of the S-A and SST turbulence models can be found in their respective references,[17,18] while a detailed description of the EASM is given in the next section.

The computer code ISAAC[26] is also employed in one portion of the current study. The ISAAC code is functionally very similar to the CFL3D code, but it possesses higher order turbulence models, including RSMs. The turbulence models in ISAAC are solved fully-coupled with the mean flow equations.

3 Algebraic Stress Model Methodology

The application of algebraic stress models (ASMs) to a variety of flow problems has become commonplace. With this increase in use has also come a variety of formulations. These formulations differ in the number of basis terms used in the tensor representation and in the particular means by which the ASM is implemented. The ASM used in this study is based on the model originally developed by Gatski and Speziale,[19] but extended and implemented based on a formulation developed by Jongen and Gatski.[27] The reader is referred to these earlier studies for additional background.

3.1 General Algebraic Stress Model

The common starting point for the development of ASMs is the modeled transport equation for the Reynolds stress tensor τ_{ij} given by

$$\frac{1}{2K}\left[\frac{D\tau_{ij}}{Dt}-\frac{\tau_{ij}}{K}\frac{DK}{Dt}\right]-\frac{1}{2K}\left[\mathcal{D}_{ij}-\frac{\tau_{ij}}{2K}\mathcal{D}_{nn}\right] = -\frac{1}{a_4}\mathbf{b}-a_3\left(\mathbf{bS}+\mathbf{Sb}-\frac{2}{3}\{\mathbf{bS}\}\mathbf{I}\right) + a_2\left(\mathbf{bW}-\mathbf{Wb}\right)-\mathbf{R}, \quad (1)$$

where $K=\frac{1}{2}\tau_{nn}$ is the turbulence kinetic energy, $\mathcal{D}_{ij}$ is the turbulent transport and viscous diffusion tensor, and $\{\mathbf{bS}\}=b_{ij}S_{ji}$ is the trace. The tensor $\mathbf{R}=a_1\mathbf{S}$ when a linear pressure-strain correlation model is assumed as well as an isotropic dissipation rate ε, but $\mathbf{R}$ can in general be any symmetric traceless tensor.[27] The kinematic strain rate and rotation rate tensors, S_{ij} and W_{ij} respectively, are

$$S_{ij}=\frac{1}{2}\left(\frac{\partial u_i}{\partial x_j}+\frac{\partial u_j}{\partial x_i}\right),\quad W_{ij}=\frac{1}{2}\left(\frac{\partial u_i}{\partial x_j}-\frac{\partial u_j}{\partial x_i}\right),$$

and the Reynolds stress anisotropy tensor is defined as

$$b_{ij}=\frac{\tau_{ij}}{2K}-\frac{1}{3}\delta_{ij}. \quad (2)$$

The coefficients a_i are directly related to the pressure-strain correlation model used in closing the stress transport equation. This study uses the SSG pressure-strain model,[28] which yields

$$a_1=\frac{1}{2}\left(\frac{4}{3}-C_2\right),\quad a_2=\frac{1}{2}(2-C_4),$$
$$a_3=\frac{1}{2}(2-C_3),\quad a_4=g\tau,\quad \tau=\frac{K}{\varepsilon}, \quad (3)$$

and

$$g = \left[\left(\frac{C_1^1}{2}+1\right)\frac{\mathcal{P}}{\varepsilon}+\frac{1}{2}C_1^0-1\right]^{-1} = \left[\gamma_0\frac{\mathcal{P}}{\varepsilon}+\gamma_1\right]^{-1}, \quad (4)$$

where $C_1^0=3.4$, $C_1^1=1.8$, $C_2=0.36$, $C_3=1.25$, and $C_4=0.4$.

An *implicit* algebraic stress relation is obtained from the modeled transport equation for the Reynolds stresses (Eq. (1)) when the following two assumptions are made:

$$\mathcal{D}_{ij}=\frac{\tau_{ij}}{2K}\mathcal{D}_{nn}, \quad (5)$$

and

$$\frac{D\tau_{ij}}{Dt}=\frac{\tau_{ij}}{K}\frac{DK}{Dt}. \quad (6)$$

Equation (6) is equivalent to requiring that the turbulence has reached an equilibrium state, $\frac{D\mathbf{b}}{Dt}=0$. With these assumptions, the left side of Eq. (1) vanishes, and the equation becomes algebraic:

$$-\frac{1}{a_4}\mathbf{b}-a_3\left(\mathbf{bS}+\mathbf{Sb}-\frac{2}{3}\{\mathbf{bS}\}\mathbf{I}\right) + a_2(\mathbf{bW}-\mathbf{Wb})=\mathbf{R}. \quad (7)$$

Equation (7) has to be solved for $\mathbf{b}$ and is an implicit equation. For the case $\mathbf{R}=a_1\mathbf{S}$, an explicit solution of Eq. (7) has been obtained by Gatski and Speziale[19] for 2-D mean flows in the form

$$\mathbf{b}=\alpha_1\mathbf{S}+\alpha_2(\mathbf{SW}-\mathbf{WS})+\alpha_3\left(\mathbf{S}^2-\frac{1}{3}\{\mathbf{S}^2\}\mathbf{I}\right), \quad (8)$$

where the α_i are scalar coefficient functions of the invariants $\eta^2 (= \{\mathbf{S}^2\})$ and $\mathcal{R}^2 (= -\{\mathbf{W}^2\}/\{\mathbf{S}^2\})$. (Here, $\mathcal{R}^2$ is a nondimensional flow parameter that is very useful for characterizing the flow;[22,29] for example, for a pure shear flow $\mathcal{R}^2 = 1$, whereas for a plane strain flow $\mathcal{R}^2 = 0$.) A new methodology for identifying the coefficients α_i, such that Eq. (8) is the solution of the general stress relation Eq. (7), will now be derived.

3.2 Explicit Solution

Consider a three-term tensor representation given by

$$\mathbf{b} = \sum_{n=1}^{3} \alpha_n \mathbf{T}^{(n)}. \tag{9}$$

with the three-term tensor basis $\mathbf{T}^{(m)}$,

$$\mathbf{T}^{(1)} = \mathbf{S}, \quad \mathbf{T}^{(2)} = \mathbf{SW} - \mathbf{WS}, \quad \mathbf{T}^{(3)} = \mathbf{S}^2 - \frac{1}{3}\{\mathbf{S}^2\}\mathbf{I}. \tag{10}$$

As discussed in Jongen and Gatski,[27] higher term bases ($N \geq 5$) are also possible, but we consider here only the three-term basis, which is exact for 2-D flows.

Equation (7) can be solved *à la Galerkin* by projecting this algebraic relation onto the tensor basis $\mathbf{T}^{(m)}$ itself. For this, we form the scalar product of Eq. (7) with each of the tensors $\mathbf{T}^{(m)}$, $(m = 1, 2, 3)$. This leads to the following system of equations:

$$\sum_{n=1}^{3} \alpha_n \left[-\frac{1}{a_4}(\mathbf{T}^{(n)}, \mathbf{T}^{(m)}) - 2a_3(\mathbf{T}^{(n)}\mathbf{S}, \mathbf{T}^{(m)}) + 2a_2(\mathbf{T}^{(n)}\mathbf{W}, \mathbf{T}^{(m)}) \right] = (\mathbf{R}, \mathbf{T}^{(m)}), \tag{11}$$

where, for example, the scalar product is defined as $(\mathbf{T}^{(n)}, \mathbf{T}^{(m)}) = \{\mathbf{T}^{(n)}\mathbf{T}^{(m)}\}$. In a more compact form,

$$\sum_{n=1}^{3} \alpha_n A_{nm} = (\mathbf{R}, \mathbf{T}^{(m)}), \tag{12}$$

where the 3×3 matrix $\mathbf{A}$ is defined as

$$A_{nm} \equiv -\frac{1}{a_4}(\mathbf{T}^{(n)}, \mathbf{T}^{(m)}) - 2a_3(\mathbf{T}^{(n)}\mathbf{S}, \mathbf{T}^{(m)}) + 2a_2(\mathbf{T}^{(n)}\mathbf{W}, \mathbf{T}^{(m)}). \tag{13}$$

In the 2-D mean velocity field case, the matrix $\mathbf{A}$ is

$$A_{nm} = \begin{bmatrix} -\frac{1}{a_4}\eta^2 & -2a_2\eta^4\mathcal{R}^2 & -\frac{1}{3}a_3\eta^4 \\ 2a_2\eta^4\mathcal{R}^2 & -\frac{2}{a_4}\eta^4\mathcal{R}^2 & 0 \\ -\frac{1}{3}a_3\eta^4 & 0 & -\frac{1}{6a_4}\eta^4 \end{bmatrix}, \tag{14}$$

which, when inverted, leads to the following expressions for the representation coefficients

$$\alpha_1 = -\frac{a_4}{\alpha_0\eta^2}\left(\{\mathbf{RS}\} + 2a_2a_4\{\mathbf{RWS}\} - 2a_3a_4\{\mathbf{RS}^2\}\right), \tag{15}$$

$$\alpha_2 = a_4\left[a_2\alpha_1 + \frac{\{\mathbf{RWS}\}}{\eta^4\mathcal{R}^2}\right], \tag{16}$$

$$\alpha_3 = -a_4\left[2a_3\alpha_1 + \frac{6\{\mathbf{RS}^2\}}{\eta^4}\right], \tag{17}$$

where $\alpha_0 = \left(1 - \frac{2}{3}a_3^2a_4^2\eta^2 + 2a_2^2a_4^2\eta^2\mathcal{R}^2\right)$. This set of equations is the general solution valid for two-dimensional mean flow and for any arbitrary (symmetric traceless) tensor $\mathbf{R}$.

As noted previously, when a linear pressure-strain correlation model is assumed as well as an isotropic dissipation rate, then $\mathbf{R} = a_1\mathbf{S}$. This expression leads to a right-hand side for Eq. (12) proportional to

$$(\mathbf{R}, \mathbf{T}^{(m)}) = \begin{bmatrix} \{\mathbf{RS}\} \\ -2\{\mathbf{RWS}\} \\ \{\mathbf{RS}^2\} \end{bmatrix} = \begin{bmatrix} a_1\eta^2 \\ 0 \\ 0 \end{bmatrix}. \tag{18}$$

This result can be related to previous formulations involving the three-term basis. From Eq. (3), the coefficient a_4 is dependent on g and as such has a direct dependency on the ratio $\mathcal{P}/\varepsilon$ from Eq. (4). The solution proposed by Gatski and Speziale[19] for the explicit algebraic stress model fixed the value of g. Using Eq. (18) in Eqs. (15)–(17) and substituting into Eq. (9) leads to the tensor representation for $\mathbf{b}$ obtained by Gatski and Speziale[19]

$$\mathbf{b} = \nu_t^*\left[\mathbf{S} + a_2a_4(\mathbf{SW} - \mathbf{WS}) - 2a_3a_4\left(\mathbf{S}^2 - \frac{1}{3}\{\mathbf{S}^2\}\mathbf{I}\right)\right], \tag{19}$$

where

$$\nu_t^* = \frac{-3a_1a_4}{3 - 2a_3^2a_4^2\eta^2 + 6a_2^2a_4^2\eta^2\mathcal{R}^2}. \tag{20}$$

In an alternative approach proposed by Ying and Canuto[20] and Girimaji,[21] the value of g is not fixed; the variation of the production-to-dissipation-rate ratio in the flow is accounted for in the formulation. This approach can also be accounted for in the present formulation. It is easily shown that the production-to-dissipation-rate ratio is given by

$$\frac{\mathcal{P}}{\varepsilon} = -2\{\mathbf{bS}\}\tau. \tag{21}$$

Previously, it has also been shown[22,27] that the invariant $\{\mathbf{bS}\}$ is directly related, for 2-D flows, to the

coefficient α_1 appearing in the tensor representation through

$$\{\mathbf{bS}\} = \alpha_1 \eta^2. \tag{22}$$

From Eqs. (3) and (4), the coefficient a_4 can then be written as

$$a_4 = \left[\gamma_1 - 2\gamma_0 \alpha_1 \eta^2 \tau\right]^{-1} \tau. \tag{23}$$

The dependency of a_4 on the production-to-dissipation-rate ratio through α_1 makes both sides of Eq. (15) functions of α_1. This dependency results in a cubic equation for α_1 given by

$$\gamma_0^2 \alpha_1^3 - \frac{\gamma_0 \gamma_1}{\eta^2 \tau} \alpha_1^2 + \frac{1}{4\eta^4 \tau^2} \left[\gamma_1^2 - 2\tau^2 \gamma_0 \{\mathbf{RS}\} - 2\eta^2 \tau^2 \left(\frac{a_3^2}{3} - \mathcal{R}^2 a_2^2 \right) \right] \alpha_1 + \frac{1}{4\eta^6 \tau} \left[\gamma_1 \{\mathbf{RS}\} + 2\tau \left(a_2 \{\mathbf{RWS}\} - a_3 \{\mathbf{RS}^2\} \right) \right] = 0. \tag{24}$$

Even with this more complicated expression for α_1, the expansion coefficients of the nonlinear terms, α_2 and α_3, retain the same functional dependency on α_1 as before. When expressed in terms of the production-to-dissipation-rate ratio with $\mathbf{R} = a_1 \mathbf{S}$, Eq. (24) can be shown[22] to be equivalent to earlier results.[20,21]

Recent results[22,30] as well as the results from this study have shown that robustness characteristics and predictive performance is improved when the variation of the production-to-dissipation-rate ratio is allowed. Thus Eq. (24) (with $\mathbf{R} = a_1 \mathbf{S}$) is currently solved for α_1. Previously,[20,21] the selection of the proper root for the solution of Eq. (24) was done on the basis of continuity arguments. Here, the proper choice for the solution root is based on the asymptotic analysis of Jongen and Gatski.[23] It was found that the root with the lowest real part leads to the correct choice for α_1. The remaining expansion coefficients α_2 and α_3 are then extracted from Eqs. (16) and (17).

The explicit tensor representation given in Eq. (9) is coupled with a K-ε two-equation model. The transport equations for the turbulent kinetic energy K and dissipation rate ε are

$$\frac{DK}{Dt} = \mathcal{P} - \varepsilon + \frac{\partial}{\partial x_k} \left[\left(\nu + \frac{\nu_t}{\sigma_K} \right) \frac{\partial K}{\partial x_k} \right], \tag{25}$$

$$\frac{D\varepsilon}{Dt} = C_{\varepsilon 1} \frac{\varepsilon}{K} \mathcal{P} - f_\varepsilon C_{\varepsilon 2} \frac{\varepsilon^2}{K} + \frac{\partial}{\partial x_k} \left[\left(\nu + \frac{\nu_t}{\sigma_\varepsilon} \right) \frac{\partial \varepsilon}{\partial x_k} \right], \tag{26}$$

where ν is the kinematic viscosity, $\nu_t = C_\mu K \tau$ is a turbulent eddy viscosity, and

$$\mathcal{P} = -\tau_{ij} \frac{\partial u_i}{\partial x_j} = -2\{\mathbf{bS}\} K, \tag{27}$$

$$f_\varepsilon = \left[1 - \exp\left(-\frac{Re_K}{10.8} \right) \right], \quad Re_K = \frac{K^{1/2} d}{\nu}, \tag{28}$$

$$\sigma_K = 1.0, \quad \sigma_\varepsilon = \frac{\kappa^2}{\sqrt{C_\mu}\,(C_{\varepsilon 2} - C_{\varepsilon 1})}, \quad \kappa = 0.41, \quad C_{\varepsilon 1} = 1.44, \quad C_{\varepsilon 2} = 1.83, \quad C_\mu = 0.096, \tag{29}$$

and d is the distance to the nearest wall. These transport equations along with the explicit tensor expansion for $\mathbf{b}$ represent the EASM used in this study.

4 Results

The U-duct configuration is shown in Fig. 1. The turn has an inner radius of $r_i = 1.91$ cm and an outer radius of $r_o = 5.72$ cm. The finest grid employed is 417×153 and extends from $x/H = -4$ upstream of the bend to $x/H = 13.12$ downstream. The minimum normal spacing at the walls is 1.0×10^{-5} cm, which yields an average y^+ value of less than 0.2. Coarser grids, used to investigate grid sensitivity, are formed from the fine grid by successively eliminating every other grid point. (The grid shown in the figure is a part of the medium-level 209×77 grid.) The nominal Mach number for this flow is $M = 0.1$, and the Reynolds number per cm is $Re = 262,467$ (which corresponds to a Reynolds number based on channel width H of 1 million).

At the upstream boundary, the u-velocity profile is set based on the experimentally measured skin friction and boundary layer thickness. It is also imperative that the turbulence quantities be set at the inflow to match the experimental levels at the same location. The K and ε values at the upstream boundary are specified in a way similar to that used by Monson et al.,[5] as follows. In the near wall region ($y^+ < 4$), the values for K are obtained from the expression $K^+ = 0.05(y^+)^2$. The peak K is specified to match experiment, and is assumed to be at $y^+ = 20$. The value of ε is computed from $\varepsilon = C_\mu^{3/4} K^{3/2} / L_m$, with $L_m = \kappa y$ in the inner region and $L_m = 0.09\delta$ in the outer region. Also at the upstream boundary, the density is specified at $\rho/\rho_{\text{ref}} = 1$, and the pressure is extrapolated from the interior of the grid. At the outflow boundary, pressure is specified at $p/p_{\text{ref}} = 1$, and all other quantities are extrapolated from the interior of the grid.

4.1 Grid Sensitivity Study

Solution sensitivity to grid density is explored in Figs. 2 through 4. Figure 2 shows the inner wall skin friction coefficient using the EASM turbulence

model on three grids. The s in this figure indicates the distance of the channel centerline from a reference point approximately 83 cm upstream of the start of the bend. Except in the separated flow region, there is very little difference between the medium and fine grid results. The coarse grid (105×39) yields significant differences from the two finer grids even outside of the separated region. Results using other turbulence models show generally similar or smaller grid sensitivities.

Flow field quantities upstream of separation generally show little or no sensitivity to grid density on the three grid levels tested. For example, Fig. 3 shows the Reynolds shear stress across the channel at 90° in the bend using two different turbulence models (u_{ref} is the nominal velocity corresponding to $M_{ref} = 0.1$, and $dist = 0$ at the inner wall). Results from all three grids are plotted in the figure; there is almost no difference in the individual results on any of the grid levels. However, at and downstream of the separated region, results do show sensitivity to the grid. Figure 4 shows the Reynolds shear stress at $x/H = 2$ downstream of the bend. For both turbulence models shown, the maximum $\overline{u'v'}$ magnitude near the inner wall increases as the grid density is increased.

For the remainder of the study, all results (with one exception) were obtained using the fine grid only. Based on the results of this grid sensitivity study, we are confident that even the medium grid level is fine enough to capture the essential physics of this case, particularly upstream of the separated region (which is our primary focus in this study). Use of the fine grid adds an additional level of confidence that any differences between computations and experiment are due to the modeled physics and not due to numerical discretization errors.

4.2 Results Using Three Turbulence Models

The three turbulence models used in this study represent three successive levels of representation in describing the development and evolution of the turbulence. The EASM represents the highest level; it is derived directly from the RSM as described above, and is implemented in a two-equation K-ε formulation. The SST model is a two-equation linear eddy-viscosity model, and the S-A model is a one-equation linear eddy-viscosity model. (The RSM, results of which are discussed below in a separate subsection, utilizes seven equations to solve for the turbulence. Its results are not included in this section because the RSM is generally too expensive and very stiff, particularly with wall-bounded flows. Therefore it is not considered to be a viable model at the present time for general use with complex configurations such as multi-element airfoils.)

All three turbulence models do an excellent job predicting the flow upstream of the turn. At $x/H = -2$, both mean flow profiles and turbulence quantities are in excellent agreement with experiment. For example, Fig. 5 shows the Reynolds shear stress at this upstream location. Near the start of the bend, at $x/H = 0$ (0°), however, computed Reynolds shear stresses are already showing significant differences from the experimentally measured levels (Fig. 6). In particular, the turbulence models all predict a positive peak near the convex inner wall followed by a negative peak further from the wall; the experiment shows only positive values in this region. Although not shown, all models at this $x/H = 0$ (0°) station still predict the turbulent kinetic energy and mean streamwise velocity in good agreement with each other and with experiment.

Figures 7, 8, and 9 show mean streamwise velocity, Reynolds shear stress, and turbulent kinetic energy, respectively, at the 90° position halfway around the bend. (Note that K is not given for S-A, because it is not explicitly computed for the one-equation model.) The results for the three turbulence models are very similar near the convex wall: none of the models predict zero (complete destruction of) Reynolds shear stress, as seen in the experiment (Fig. 8). In the outer half of the channel, all models underpredict the magnitude of both $\overline{u'v'}$ and K. However, the EASM predicts higher levels than the two eddy viscosity models, in better agreement with experiment. The poor predictions of the turbulence quantities at the 90° station in the bend do not affect the predictions of the mean velocity profiles there. All models predict similar velocity profiles (Fig. 7). Overall, these results are in reasonable agreement with experiment, although the velocity magnitude near the inner wall is slightly overpredicted and the velocity magnitude near the outer wall is underpredicted.

Separation and reattachment locations are given in Table 1. Results from Luo and Lakshminarayana[11] are also shown for comparison. The S-A, SST, and EASM all predict the separation location too far downstream in comparison with experiment, but predict comparable separation lengths in agreement with the upper range of the data. Separated velocity profiles are shown in Fig. 10 at location $x/H = 0.5$. None of the models predict the correct magnitude of maximum reverse flow, but the EASM does the best job predicting the overall mean flow profile.

Downstream of reattachment, the flow field recovers from the effects of separation. Considering that

none of the models predict the turbulence correctly in the bend, predictions downstream are likely to be incorrect anyway (because each model is "recovering" from incorrect upstream levels). Therefore, in the interest of conserving space, we do not show these results here. The results are quantitatively very similar to the NL K-ε and ARSM results shown in Ref. 11. We do note, however, that all three of the turbulence models exhibit a too-slow recovery from separation. This trend was also noted in Ref. 11, and is a well-recognized feature of most turbulence models in use today.[31]

Pressure coefficients along the inner and outer wall are shown in Figs. 11 and 12, and skin friction coefficients are shown in Figs. 13 and 14. Overall, the EASM predicts these levels downstream of the bend in better agreement with experiment than the predictions of the other models.

4.3 EASM Analysis

The EASM used in this study accounts for the variation of the production-to-dissipation-rate ratio; i.e., g (Eq. (4)) is variable. As will be shown, if g is held constant at 0.233 (corresponding to the equilibrium value of $\mathcal{P}/\varepsilon = 1.886$ for homogeneous shear flow), predictions of turbulence quantities in the curvature region of this flow field are poor.

For example, computed Reynolds shear stresses at 90° in the bend using EASM with constant $g = 0.233$ are shown in Fig. 15 in comparison with results from the variable g model. The constant g model dramatically overpredicts the magnitudes of $\overline{u'v'}$ near the inner wall in this region. (K, not shown, is also significantly overpredicted near the convex wall.) This behavior is very similar to that exhibited by the eddy viscosity K-ε model used by Luo and Lakshminarayana.[11] The constant g model also yields a significantly smaller region of separation ($s/H = 1.34$) in comparison with the other models. The separation angle is 171° and reattachment occurs at $x/H = 1.26$.

As shown in Fig. 16, the computed value of $\mathcal{P}/\varepsilon$ is far from 1 (which is the equilibrium value in the log-layer of a channel flow) over much of the channel *outside* of the inner-wall log-layer at the stations where curvature is present. Figure 17 is a plot of the flow parameter $\mathcal{R}^2$ as a function of y^+ at the same three locations shown in the previous figure. At the $x/H = -2$ station well upstream of the bend, $\mathcal{R}^2 \approx 1$ (except in the middle of the channel), representing pure shear flow, as expected. Also, $\mathcal{R}^2 \approx 1$ within the lower part of the log-layers at all three stations. However, $\mathcal{R}^2$ deviates significantly from 1 for the flow outside $y^+ \approx 500$ at the two stations in the bend. At both locations, $\mathcal{R}^2$ approaches 0 at large y^+, representing plane strain flow.

Figures 18 and 19 show plots of $\eta\tau$ as a function of $\mathcal{P}/\varepsilon$ for the EASM with variable g and constant g, respectively. The symbols show the computed values, and the solid and dashed lines show the theory[22] for two cases of $\mathcal{R}^2 = 0$ and $\mathcal{R}^2 = 1$. Comparing these two figures, it is seen that the computed levels for each model (most of whose values of $\mathcal{R}^2$ are near either 0 or 1) agree well with the theory, as they should. Furthermore, the theoretical curves for the two models are very similar for roughly $\eta\tau < 4$, but they deviate significantly above this level. For this flow, in the straight-wall sections of the duct or in the near-wall log-layer region where $\mathcal{R}^2 \approx 1$, $\eta\tau$ remains less than 4 and the two models behave similarly. However, the two models behave quite differently outside of the log-layer in the curved section of the duct where $\mathcal{R}^2$ approaches 0, because $\eta\tau$ can be considerably larger than 4 there. Because α_1 is proportional to $-(\mathcal{P}/\varepsilon)/\eta^2$ (from Eqs. (21) and (22)), the EASM with constant g predicts significantly larger levels of ν_t^* outside the log-layer in the curved region of the flow than EASM with variable g. This is the source of the larger predicted $\overline{u'v'}$ peak near the inner wall for EASM (constant g) in Fig. 15.

4.4 Comparison with RSM

Finally, the U-duct flow is solved with an RSM using the ISAAC code on the 209×77 grid. Our focus is not to compare global results, but rather to explore in detail the behavior near convex curvature. Results at 90° in the bend are shown in comparison with the EASM result using CFL3D in Fig. 20. (Although not shown, EASM in ISAAC yields results similar to those of EASM in CFL3D.) The RSM successfully suppresses the Reynolds shear stress near the inner wall, in better agreement with experiment. These results are also consistent with Ref. 11. Figure 21 compares the locus of solution points for RSM with those of EASM at 90° in the bend. For clarity, only points at which $\mathcal{R}^2$ is close to zero are shown (RSM and EASM give very similar results within the log-layer, where $\mathcal{R}^2$ is close to 1). It is clear that the EASM is not mimicking the RSM outside the log-layer in the curvature region.

Evidently, one or more of the assumptions that go into the derivation of the EASM is causing the model to deviate from the RSM result for this flow in the curvature region. Recall that two of the primary assumptions in developing the algebraic relationship are given in Eqs. (5) and (6). Therefore, we scrutinize the computed levels of each of these

terms from the RSM solution. Figure 22 shows contours of Db_{11}/Dt (nondimensionalized by L/a_∞) near the start of the bend. Other Db_{ij}/Dt terms are of similar magnitude. Near $x = 0$ (0° in the bend), Db_{11}/Dt is negative (at a maximum level of about -0.01), followed by a positive peak at a maximum of approximately 0.012 somewhat downstream. These levels of Db_{11}/Dt are of the same order of magnitude as the nondimensional $a_1 S_{11}$ levels at the same locations (Fig. 23), which indicates that the first term in Eq. (1) ($= D\mathbf{b}/Dt$) is probably important in this region of the flow and should not be neglected. Although not shown, the $\mathcal{D}_{ij} - (\tau_{ij}/2K)\mathcal{D}_{nn}$ terms computed from the RSM solution are very small in comparison with the $D\mathbf{b}/Dt$ terms, of order 10^{-8}. Therefore, it is not expected that neglecting them in the derivation of the EASM has any impact for this flow field.

5 Conclusions

The abilities of three types of turbulence models to predict 2-D curvature effects, which may be important for high-lift flow fields, were investigated for a model test problem. It was shown that an explicit algebraic stress model performs better than one- or two-equation eddy viscosity models, provided that the variation of the production-to-dissipation-rate ratio in the flow is accounted for in the formulation. Surface pressure and skin friction were also predicted best by this model. Theoretical analysis of the explicit algebraic stress model provided some insight into the differences in the behavior of this model in the curved region of the flow when g is held constant.

None of the one- or two-equation turbulence models used in this study captured the full extent of suppressed turbulence near the convex wall or enhanced turbulence near the concave wall. However, a full Reynolds stress turbulence model successfully suppressed turbulence near the convex wall. Some of the assumptions that go into the derivation of the explicit algebraic stress model were investigated and compared with the computed flow field from the full Reynolds stress model. Through this analysis, the algebraic model assumption that $Db_{ij}/Dt = 0$ was found to be suspect in the strong curvature region.

References

1. Lynch, F. T., Potter, R. C., and Spaid, F. W., "Requirements for Effective High Lift CFD," *International Council of the Aeronautical Sciences (ICAS) proceedings, 20th Congress*, Vol. 2, AIAA, Reston, VA, 1996, pp. 1479–1492.

2. Ying, S. X., Spaid, F. W., McGinley, C. B., and Rumsey, C. L., "Investigation of Confluent Boundary-Layers in High-Lift Flow," AIAA Paper 98-2622, June 1998.

3. Patel, V. C., and Sotiropoulos, F., "Longitudinal Curvature Effects in Turbulent Boundary Layers," *Prog. Aerospace Sci.*, Vol. 33, 1997, pp. 1–70.

4. Monson, D. J., and Seegmiller, H. L., "An Experimental Investigation of Subsonic Flow in a Two-Dimensional U-Duct," NASA TM 103931, July 1992.

5. Monson, D. J., Seegmiller, H. L., McConnaughey, P. K., and Chen, Y. S., "Comparison of Experiment with Calculations Using Curvature-Corrected Zero and Two-Equation Turbulence Models for a Two-Dimensional U-Duct," AIAA Paper 90-1484, June 1990.

6. So, R. M. C., and Mellor, G. L., "Experiment on Convex Curvature Effects in Turbulent Boundary Layers," *J. Fluid Mech.*, Vol. 60, Part 1, 1973, pp. 43–62.

7. Gillis, J. C., and Johnston, J. P., "Turbulent Boundary-Layer Flow and Structure on a Convex Wall and its Redevelopment on a Flat Wall," *J. Fluid Mech.*, Vol. 135, 1983, pp. 123–153.

8. Kim, W. J., and Patel, V. C., "An Experimental Study of Boundary-Layer Flow in a Curved Rectangular Duct," *ASME Fluids Engineering Conference*, FED-Vol. 146, American Society of Mechanical Engineers, New York, 1993, pp. 13–28.

9. Launder, B. E., and Loizou, P. A., "Laminarization of Three-Dimensional Accelerating Boundary Layers in a Curved Rectangular-Sectioned Duct," *Int. J. Heat and Fluid Flow*, Vol. 13, No. 2, 1992, pp. 124–131.

10. Schwarz, A. C., and Plesniak, M. W., "Convex Turbulent Boundary Layers with Zero and Favorable Pressure Gradients," *J. of Fluids Engineering*, Vol. 118, Dec. 1996, pp. 787–794.

11. Luo, J., and Lakshminarayana, B., "Prediction of Strongly Curved Turbulent Duct Flows with Reynolds Stress Model," *AIAA Journal*, Vol. 35, No. 1, 1997, pp. 91–98.

12. Rodi, W., and Scheuerer, G., "Calculation of Curved Shear Layers with Two-Equation Turbulence Models," *Phys. Fluids*, Vol. 26, No. 6, 1983, pp. 1422–1436.

13. Luo, J., and Lakshminarayana, B., "Analysis of Streamline Curvature Effects on Wall-Bounded Turbulent Flows," *AIAA Journal*, Vol. 35, No. 8, 1997, pp. 1273–1279.

14. Iacovides, H., Launder, B. E., Loizou, P. A., and Zhao, H. H., "Turbulent Boundary-Layer Development Around a Square-Sectioned U-Bend: Measurements and Computation," *J. of Fluids Engineering*, Vol. 112, Dec. 1990, pp. 409–415.

15. Shima, N., "Prediction of Turbulent Boundary Layers with a Second-Moment Closure: Part II – Effects of Streamline Curvature and Spanwise Rotation," *J. of Fluids Engineering*, Vol. 115, Mar. 1993, pp. 64–69.

16. Rumsey, C. L., Gatski, T. B., Ying, S. X., and Bertelrud, A., "Prediction of High-Lift Flows Using Turbulent Closure Models," *AIAA Journal*, Vol. 36, No. 5, 1998, pp. 765–774.

17. Spalart, P. R., and Allmaras, S. R., "A One-Equation Turbulence Model for Aerodynamic Flows," *La Recherche Aerospatiale*, No. 1, 1994, pp. 5–21.

18. Menter, F. R., "Improved Two-Equation k-ω Turbulence Models for Aerodynamic Flows," NASA TM 103975, Oct. 1992.

19. Gatski, T. B., and Speziale, C. G., "On Explicit Algebraic Stress Models for Complex Turbulent Flows," *J. Fluid Mech.*, Vol. 254, 1993, pp. 59–78.

20. Ying, R., and Canuto, V. M., "Turbulence Modelling over Two-Dimensional Hills Using an Algebraic Reynolds Stress Expression," *Boundary-Layer Meteorology*, Vol. 77, 1996, pp. 69–99.

21. Girimaji, S. S., "Fully Explicit and Self-Consistent Algebraic Reynolds Stress Model," *Theoret. Comput. Fluid Dynamics*, Vol. 8, 1996, pp. 387–402.

22. Jongen, T., and Gatski, T. B., "A New Approach to Characterizing the Equilibrium States of the Reynolds Stress Anisotropy in Homogeneous Turbulence," *Theoret. Comput. Fluid Dynamics*, Vol. 11, 1998, pp. 31–47. Erratum: *Theoret. Comput. Fluid Dynamics*, Vol. 12, 1998, pp. 71–72.

23. Jongen, T., and Gatski, T. B., "Time Evolution of Modeled Reynolds Stresses in Planar Homogeneous Flows," NASA TM-97-206265, Dec. 1997.

24. Krist, S. L., Biedron, R. T., and Rumsey, C. L., "CFL3D User's Manual (Version 5.0)," NASA TM-1998-208444, June 1998.

25. Roe, P. L., "Approximate Riemann Solvers, Parameter Vectors, and Difference Schemes," *J. Comput. Phys.*, Vol. 43, 1981, pp. 357–372.

26. Morrison, J. H., "A Compressible Navier-Stokes Solver With Two-Equation and Reynolds Stress Turbulence Closure Models," NASA CR-4440, May 1992.

27. Jongen, T., and Gatski, T. B., "General Explicit Algebraic Stress Relations and Best Approximation for Three-Dimensional Flows," *Int. J. Engr. Sci.*, Vol. 36, 1998, pp. 739–763.

28. Speziale, C. G., Sarkar, S., and Gatski, T. B., "Modeling the Pressure-Strain Correlation of Turbulence: an Invariant Dynamical Systems Approach," *J. Fluid Mech.*, Vol. 227, 1991, pp. 245–272.

29. Astarita, G., "Objective and Generally Applicable Criteria for Flow Classification," *J. Non-Newtonian Fluid Mech.*, Vol. 6, 1979, pp. 69–76.

30. Jongen, T., Machiels, L., and Gatski, T. B., "Predicting Noninertial Effects with Linear and Nonlinear Eddy-Viscosity and Algebraic Stress Models," *Flow, Turbulence and Combustion*, To Appear, 1999.

31. Johnson, D. A., Menter, F. R., and Rumsey, C. L., "The Status of Turbulence Modeling for External Aerodynamics," AIAA Paper 94-2226, June 1994.

Table 1. **Location and extent of separation**

	Sep. θ, deg.	Reattach. x/H	Sep. len. L/H
S-A	170	1.72	1.81
SST	164	1.57	1.71
EASM	164	1.56	1.70
K-ε[11]	172	0.72	0.79
NL K-ε[11]	163	1.30	1.45
ARSM[11]	157	1.62	1.82
RSM[11]	147	1.55	1.84
Data[4]	150	1.0–1.5	1.26–1.76

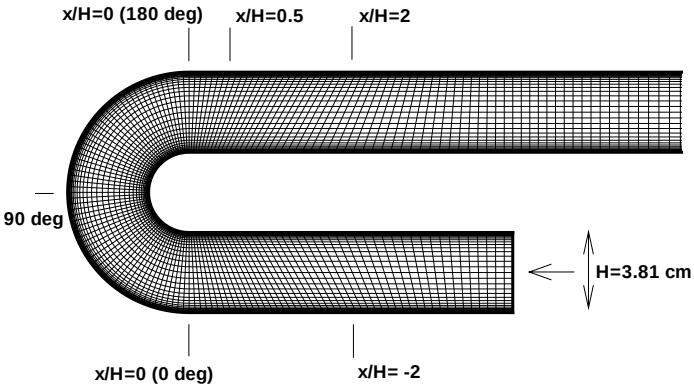

Figure 1. U-duct configuration (portion of 209×77 grid shown).

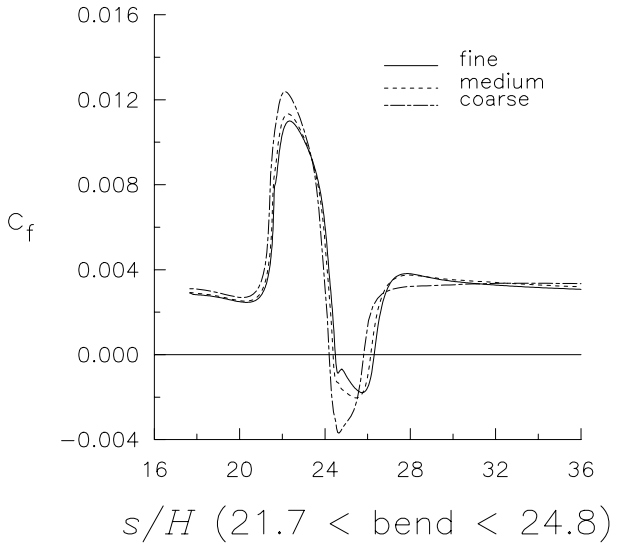

Figure 2. Effect of grid density on inner surface skin friction using EASM.

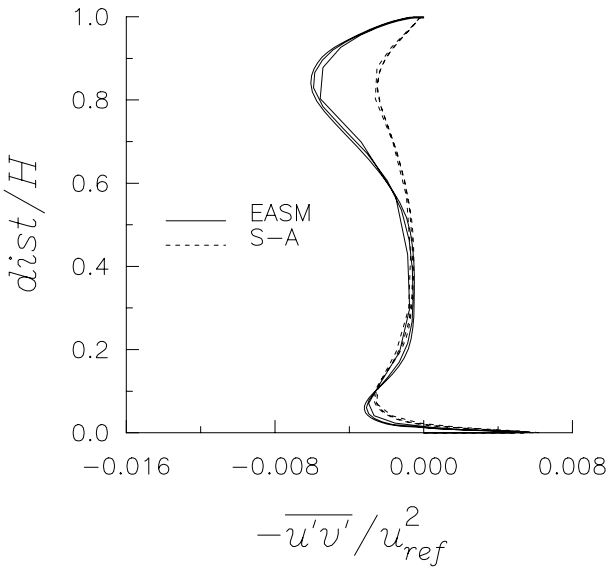

Figure 3. Computed Reynolds shear stress on coarse, medium, and fine grids for each of two turbulence models at 90° in the bend.

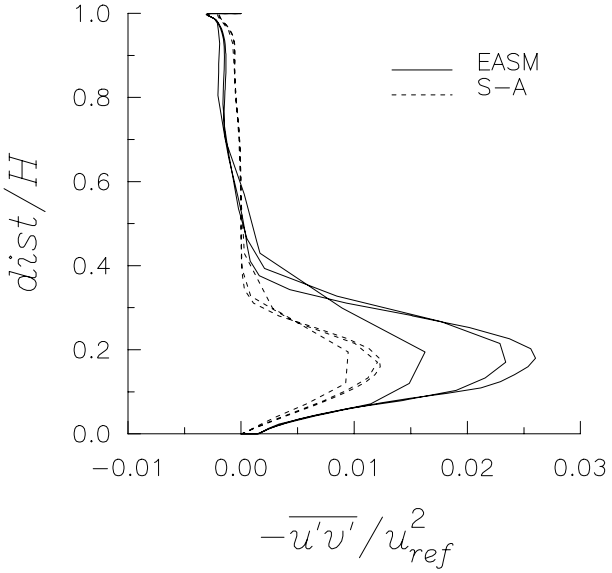

Figure 4. Computed Reynolds shear stress on coarse, medium, and fine grids for each of two turbulence models at $x/H = 2$.

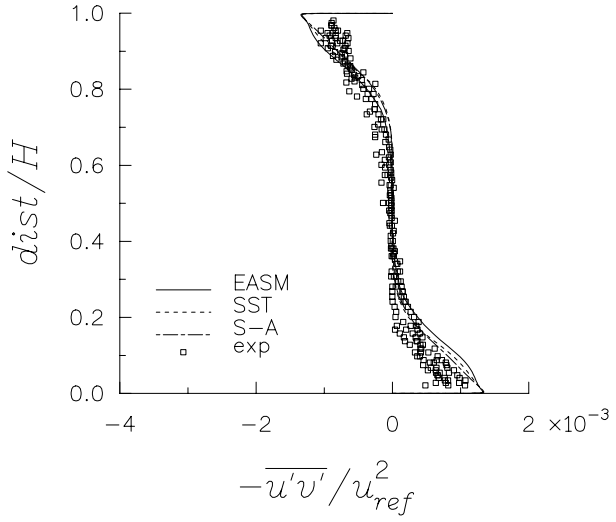

Figure 5. Turbulent Reynolds shear stress at $x/H = -2$.

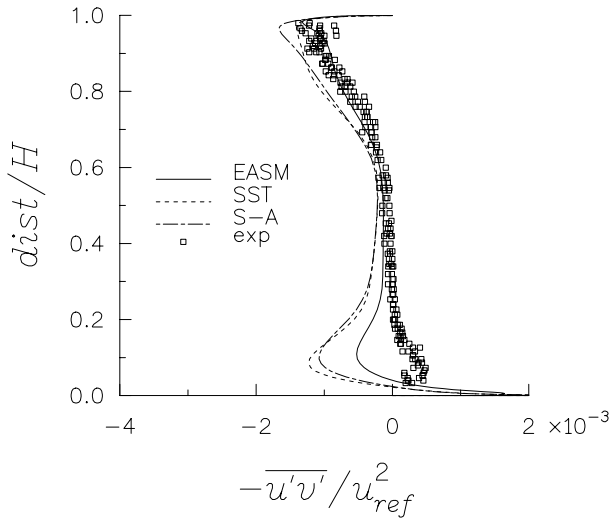

Figure 6. Turbulent Reynolds shear stress at 0° in the bend.

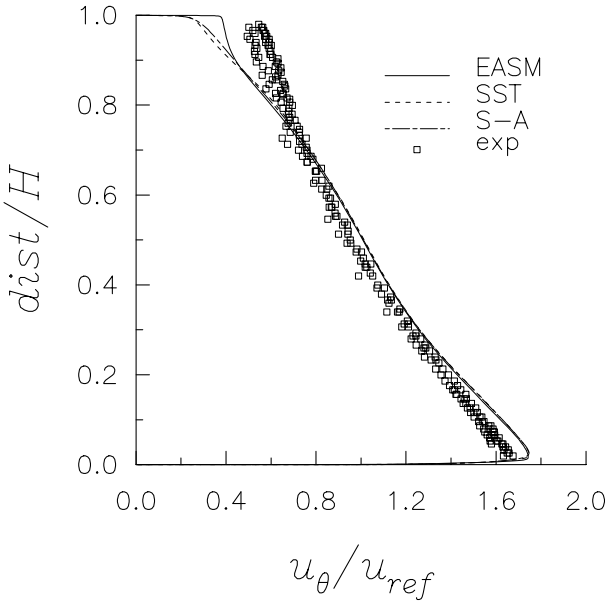

Figure 7. Streamwise velocity at 90° in the bend.

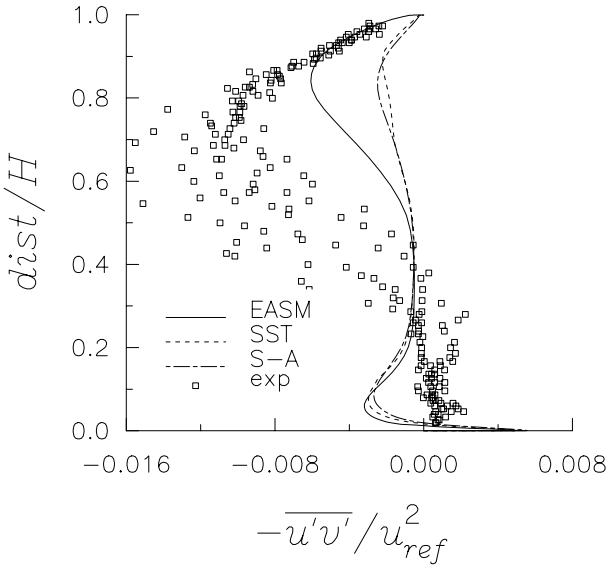

Figure 8. Turbulent Reynolds shear stress at 90° in the bend.

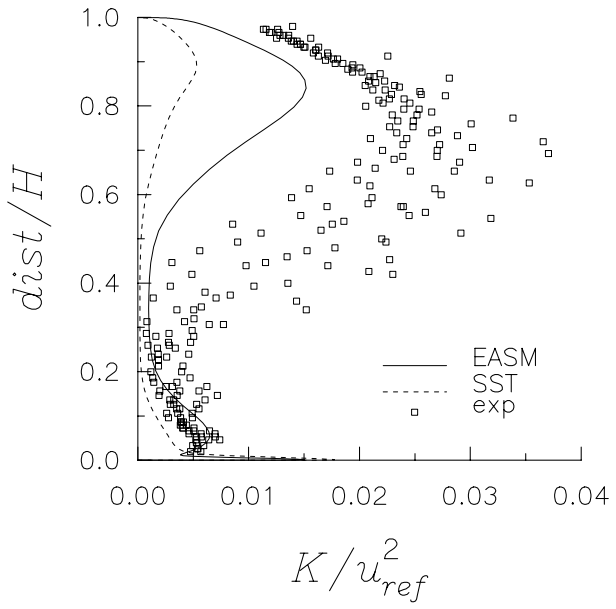

Figure 9. Turbulent kinetic energy at 90° in the bend.

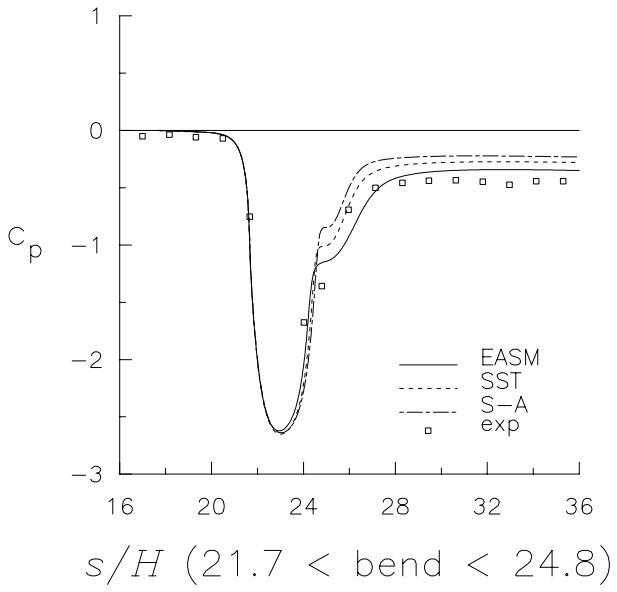

Figure 11. Inner surface pressure coefficient.

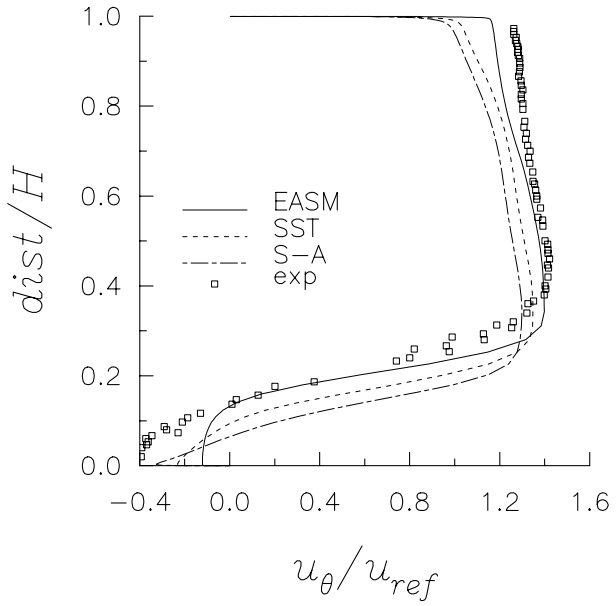

Figure 10. Streamwise velocity at $x/H = 0.5$ in the separated region.

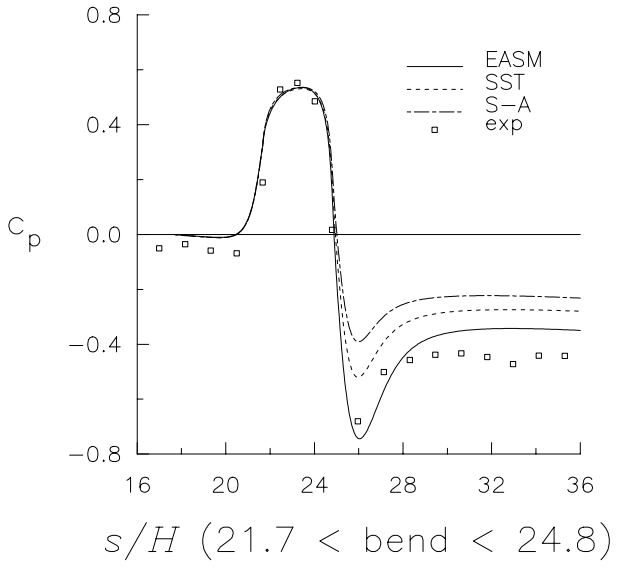

Figure 12. Outer surface pressure coefficient.

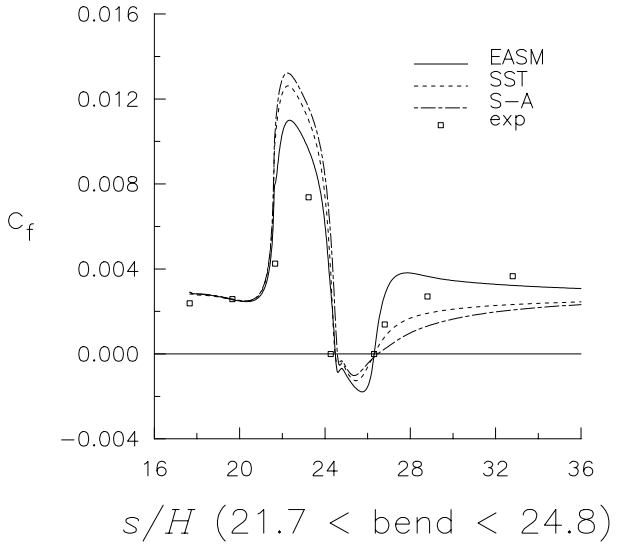

Figure 13. Inner surface skin friction coefficient.

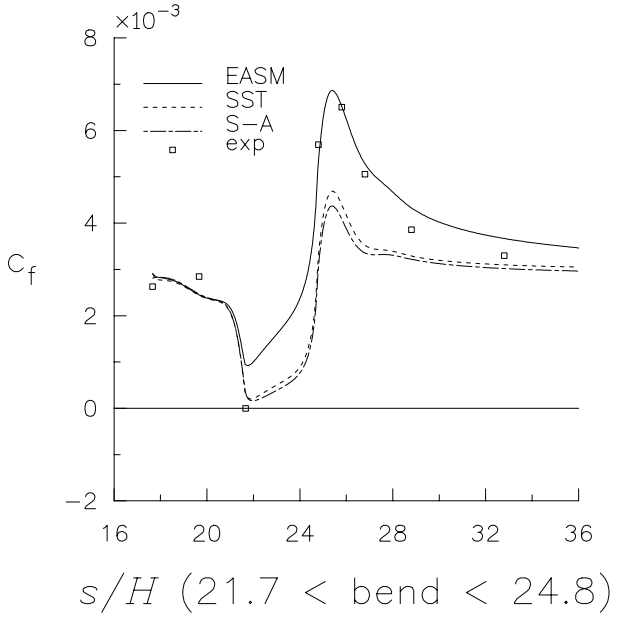

Figure 14. Outer surface skin friction coefficient.

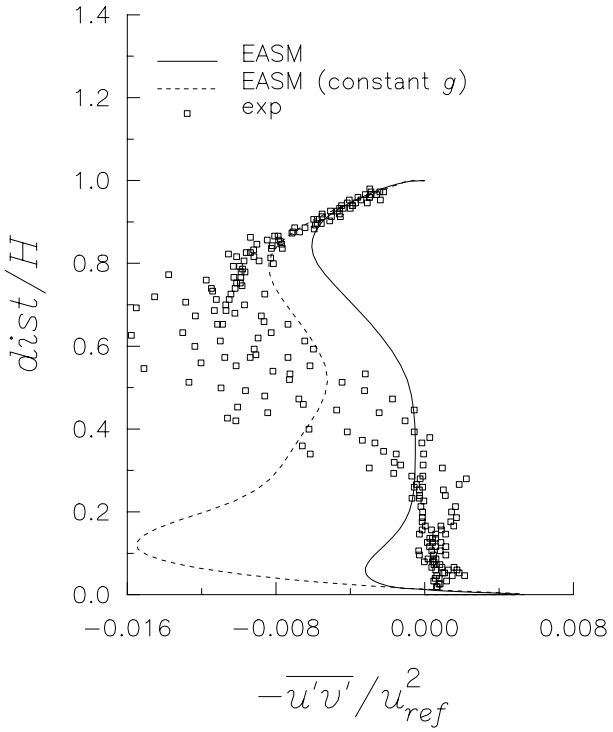

Figure 15. Effect of constant $g = 0.233$ (Ref. 19) in EASM on the Reynolds shear stress at 90° in the bend.

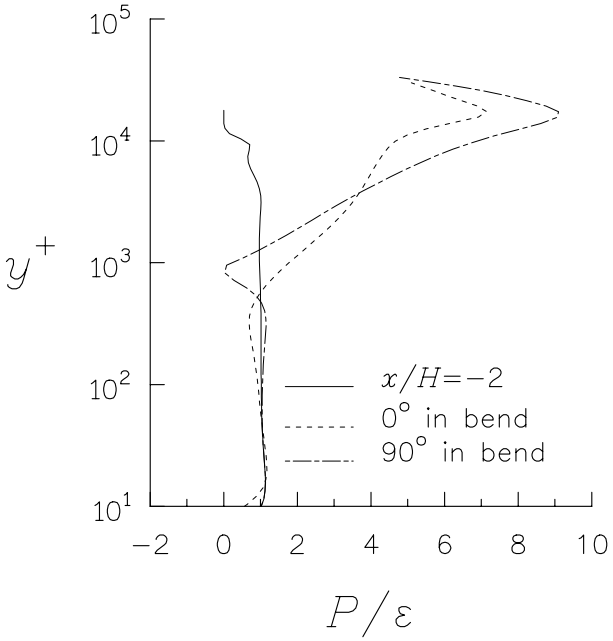

Figure 16. Production-to-dissipation-rate ratio near the inner wall computed at three stations.

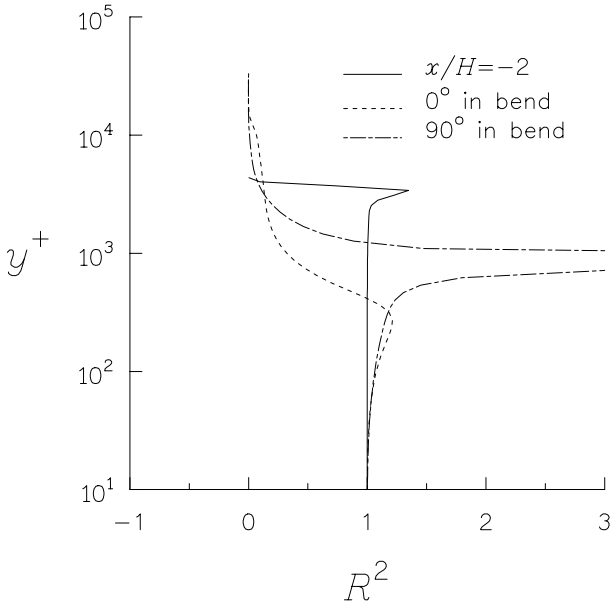

Figure 17. $\mathcal{R}^2$ levels near the inner wall computed at three stations.

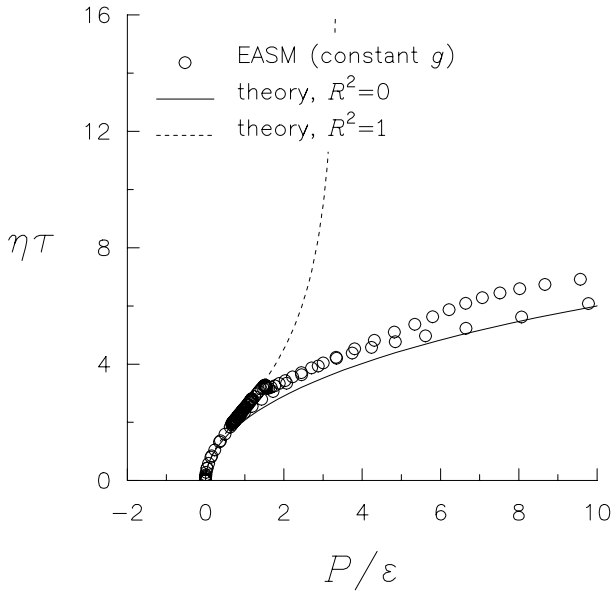

Figure 19. Locus of solution points at 0° in the bend using EASM (constant $g = 0.233$, Ref. 19).

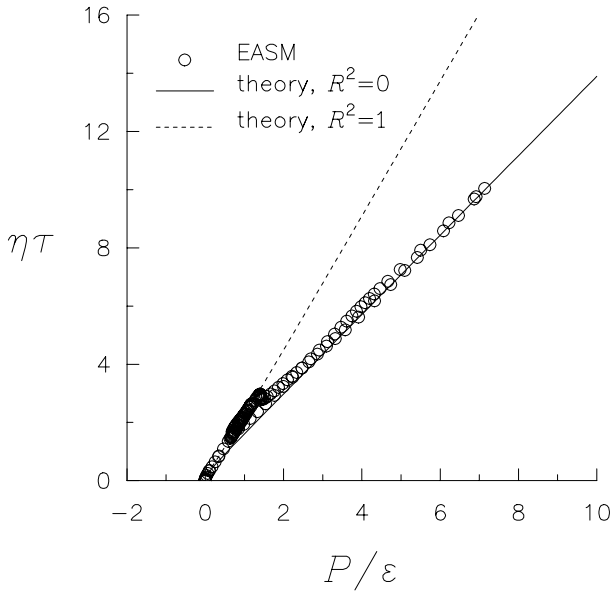

Figure 18. Locus of solution points at 0° in the bend using EASM (variable g, Eq. (4)).

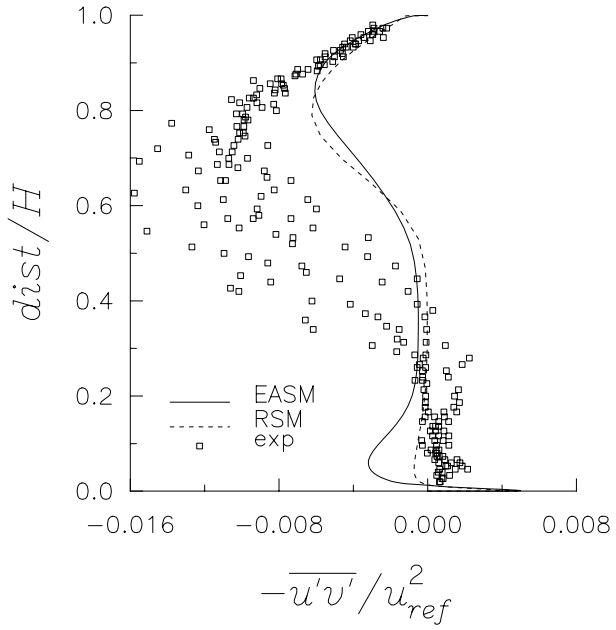

Figure 20. Comparison of RSM with EASM on the Reynolds shear stress at 90° in the bend.

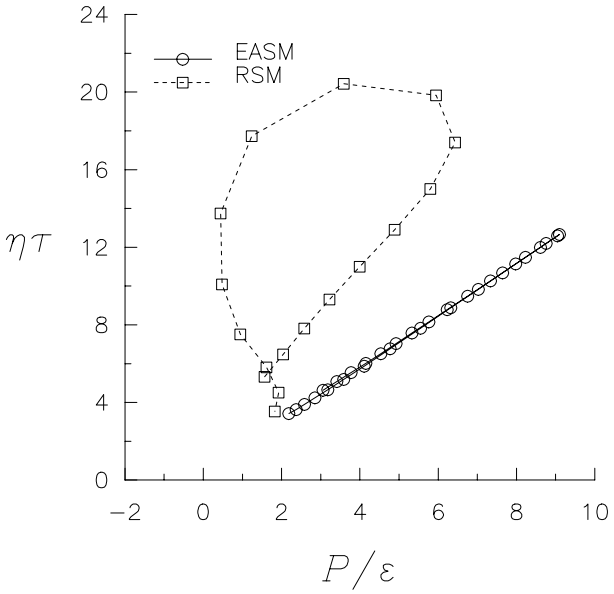

Figure 21. Locus of solution points at 90° in the bend using EASM and RSM (only points at which $\mathcal{R}^2 < 0.2$ are shown).

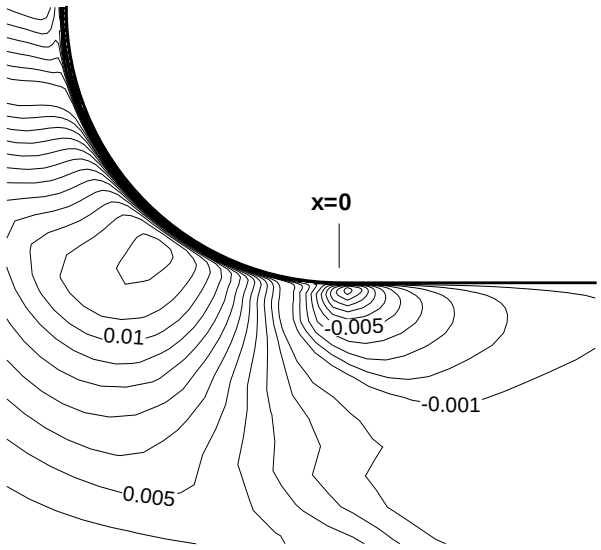

Figure 22. Contour plot of Db_{11}/Dt in the vicinity of the start of curvature using RSM (flow is from right to left).

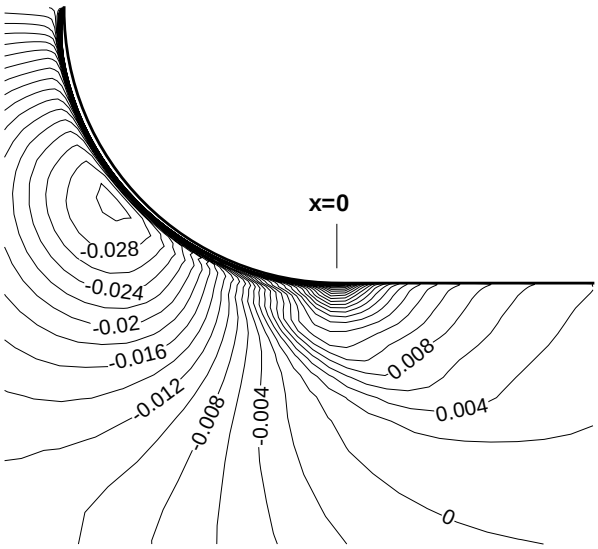

Figure 23. Contour plot of $a_1 S_{11}$ in the vicinity of the start of curvature using RSM (flow is from right to left).